Numerical study on the structural response of blast-loaded thin aluminium and steel plates

V. Aune , G. Valsamos , F. Casadei , M. Larcher , M. Langseth , T. Børvik

PII: S0734-743X(16)30248-2
DOI: 10.1016/j.ijimpeng.2016.08.010
Reference: IE 2746

To appear in: *International Journal of Impact Engineering*

Received date: 9 May 2016
Revised date: 20 August 2016
Accepted date: 21 August 2016

Please cite this article as: V. Aune , G. Valsamos , F. Casadei , M. Larcher , M. Langseth , T. Børvik , Numerical study on the structural response of blast-loaded thin aluminium and steel plates, *International Journal of Impact Engineering* (2016), doi: 10.1016/j.ijimpeng.2016.08.010

Highlight

- The inelastic response of blast-loaded thin plates is studied numerically
- Numerical simulations are validated against experimental data
- The negative phase dominated the response at some loading and structural conditions
- The influence of the negative phase was found to depend on the timing and magnitude of the peak negative pressure
- Ductile failure was also predicted by using an energy-based failure criterion

Numerical study on the structural response of blast-loaded thin aluminium and steel plates

V. Aune[a,b,*], G. Valsamos[c], F. Casadei[c,1], M. Larcher[c], M. Langseth[a,b] and T. Børvik[a,b]

[a] *Structural Impact Laboratory (SIMLab), Department of Structural Engineering, NTNU, Norwegian University of Science and Technology, NO-7491 Trondheim, Norway*

[b] *Centre for Advanced Structural Analysis (CASA), NTNU, Norwegian University of Science and Technology, NO-7491 Trondheim, Norway*

[c] *European Commission, Joint Research Centre (JRC), Institute for the Protection and Security of the Citizen (IPSC), European Laboratory for Structural Assessment (ELSA), 21027 Ispra, Italy*

Abstract

The inelastic response of thin aluminium and steel plates subjected to airblast loading is studied numerically and validated against experimental data. Special focus is placed on the influence of elastic effects and negative phase on the structural response. The blast loading was varied by detonating spherical charges of plastic explosives at various stand-off distances relative to the centre point of the plates. The numerical results obtained with the finite element code EUROPLEXUS were in good agreement with the experiments and predicted the entire range of structural response from complete tearing at the supports to a more counter-intuitive behaviour (CIB) where the final configuration of the plate was in the opposite direction to the incident blast wave due to reversed snap buckling (RSB). RSB attracted special attention since this is an unstable configuration sensitive to small changes in the loading and in structural characteristics. The negative phase of the blast pressure is usually neglected in blast-resistant design. However, the numerical simulations showed that the negative overpressure dominated the structural response and led to RSB at some loading and structural conditions. Two distinctive types of CIB were identified and both were found to depend on the timing and magnitude of the peak negative overpressure relative to the dynamic response of the plates. The study also revealed that CIB may occur in thin plates when the negative impulse is of the same order of magnitude as the positive impulse. The partial and complete failure along the boundaries observed in some of the tests was also successfully recreated in the simulations by using an energy-based failure criterion and element erosion.

Keywords: Airblast loading, reversed snap buckling, negative phase, ductile failure, EUROPLEXUS

* Corresponding author. Tel.: + 47-73-59-47-05; fax: + 47-73-59-47-01.

E-mail address: vegard.aune@ntnu.no (V. Aune).

[1] Retired.

1. Introduction

In blast-resistant design of protective structures the focus is usually on the structural response due to the positive phase of the blast loading (see [1][2][3][4][5]). This is particularly the case for small values of the scaled distance, resulting in high magnitudes of overpressure. In such events the structure is expected to deform in the same direction as the incoming blast wave, i.e., in the intuitive direction.

The positive phase of the blast wave is characterized by an almost instantaneous rise (within the timescale of nanoseconds) from atmospheric pressure p_0 to a peak incident overpressure $p_{\mathrm{so,max}}$ followed by an exponential decay in pressure back to the ambient pressure p_0 (see Figure 1). The positive phase has short time duration t_{d+} (typically milliseconds). When the blast wave interacts with a structure that is not parallel to the direction of the wave, it is reflected and reinforced. This is known as the peak reflected overpressure $p_{\mathrm{r,max}}$ and the reflected blast wave has the same general shape as the incident wave. The magnitude, duration and distribution of the blast load are a function of the explosive properties (i.e., the explosive material, weight W and shape), the location of the detonation relative to the structure (i.e., the stand-off distance R), potential objects located between the detonation and the structure, and finally the magnitude and amplification of the pressure by its interaction with the ground or the structure itself.

Some well-established references for the properties of the positive phase from an ideal airblast are the works by Kingery and Bulmash [6] and Kinney and Graham [7]. Kingery and Bulmash [6] used a large range of experimental data from spherical and hemispherical charges which were curve-fitted to high-order polynomials representing the necessary blast parameters of a TNT equivalent charge using Hopkinson-Cranz scaling ($Z = R/W^{1/3}$) [8]. However, these empirical equations are only valid in the experimental range in which they

were obtained. In particular, the data in [6] were limited to blast wave interactions with plane and infinite reflecting surfaces and contained limited data for blast parameters at scaled distances beyond the range of $0.40\ \text{m/kg}^{1/3} < Z < 40\ \text{m/kg}^{1/3}$. Some of the parameters were therefore extrapolated to smaller distances using the available data and theoretical considerations. These experiments and empirical equations form the basis for various simplified tools to predict blast loading from a given explosive weight W at a known distance R from the target, where the most commonly used tool is known as the Conventional Weapons Effects Program (ConWep) [1]. When the parameters governing the positive phase are known, the modified Friedlander equation [9][10] with an exponential decay coefficient is typically used to represent the pressure-time history. Karlos et al. [11] reviewed several approaches for calculating the exponential decay parameter and suggested new polynomial equations in determining this parameter for spherical and hemispherical charge conditions.

As the blast wave expands, the pressure decays back to ambient pressure p_0 and a negative phase occurs (where the pressure is below p_0) which typically has a longer duration t_{d-} than the positive phase. The negative phase results from the momentum of air which generates an overexpansion so that the absolute pressure at the tail of the blast wave falls below atmospheric pressure (see Figure 1). This underpressure slows down the surrounding gas molecules, producing a reversed flow back towards the explosion centre. The most commonly used negative phase parameters seem to be those given in the traditional diagrams in Reference [2]. However, there still seems to be some uncertainty regarding the modelling and treatment of the negative phase of the pressure-time history. The literature reveals three basic representations of the pressure-time history when modelling this phase, i.e., a bilinear approximation [2][12][13], an extended Friedlander equation based on the waveform of the positive phase [14][15][16] and a cubic representation [17][18][19][20][21]. Rigby et al. [20] reviewed the existing methods in representing the negative phase and discussed the

consequences of choosing an inappropriate model. Pressure measurements of a blast wave from a hemispherical charge acting on a rigid target were used to validate the proposed methods, and it was found that bilinear and cubic representations of the negative phase resulted in the best agreement with experimental data. Moreover, by using an elastic SDOF system it was shown that the dynamic response was highly dependent on an accurate description of the negative part of the pressure-time history. Bryant et al. [21] used a cubic representation of the negative phase and investigated its influence on the response of blast-loaded reinforced concrete panels and flexible metal wall systems. The negative phase was found to either mitigate or dominate the structural response depending on the timing and pressure magnitude relative to the dynamic response of the structure. Krauthammer and Altenberg [12] followed the recommendations in Reference [2] and used a piecewise linear representation of the pressure-time history to investigate the influence of the negative phase on glass panels. Their numerical study indicated that the negative phase dominated the structural behaviour for relatively small pressures, when the peak reflected overpressure was of similar magnitude to the peak negative overpressure. The influence of the negative phase was also found to depend on the dynamic characteristics of the flexible panel relative to the explosive load. In particular, the negative phase was found to dominate the response if it occurred during the elastic rebound.

Enhancement of the elastic rebound after maximum deflection was also observed experimentally by Galiev [22] for blast-loaded aluminium plates, while a comprehensive review on the influence of elastic effects during the rebound of flexible structures was performed by Yu [23]. The dynamic elastoplastic response under impulsive loading is often divided into three categories depending on the intensity of the loading and on the permanent mid-point deflection (Yu [23] and Li et al. [24]). The first two types of response are characterized by an intuitive response where the permanent mid-point deflection is in the

same direction as the incident blast wave, while the last type is often denoted counter-intuitive behaviour (CIB) because the structure first deforms in the same direction as the loading and then rebounds to a final configuration in the opposite direction. This behaviour is found to occur within a narrow range of loading and structural conditions during the transition from elastic to moderately plastic deformation and is frequently referred to as reversed snap buckling (RSB) [25]. The experiments found in the literature observing CIB due to RSB mainly consider projectile impacts where there is no negative loading phase [24][25][26] or blast events where only the positive phase is considered [27].

Aune et al. [28] investigated the effect of stand-off distance on thin aluminium and steel plates experimentally, and observed CIB and RSB at relatively small scaled distances. RSB attracted special attention as it occurred both during and after the elastic rebound. However, since it was challenging to conclude on the effects producing this abnormal response based on the experimental data in [28], the influence of the negative phase and the elastic effects on the structural response is investigated numerically in the present study using negative phase parameters and pressure-time representations proposed in the literature. This is often called an uncoupled approach and makes the inherent assumption that the blast properties are unaltered by the structural motion and the surroundings [29]. The uncoupled approach is usually the preferred procedure in blast-resistant design [2], due to the increased complexity and computational costs when using fully coupled fluid-structure interaction simulations. The numerical simulations were performed by the finite element (FE) code EUROPLEXUS (EPX) [30] using a Lagrangian formulation. The numerical model was first validated against the experimental data before a numerical study was performed to determine the combinations of stand-off distance and plate thickness resulting in RSB.

2. Experimental tests

2.1. Materials

The 0.8 mm thick plates were manufactured from the low-strength aluminium alloy EN AW 1050A-H14 and the medium-strength steel Docol 600 DL. Aune et al. [28] presented results from tensile tests on standard dog-bone specimens of both materials and used this data to determine the quasi-static behaviour. The results are plotted in Figure 2 as nominal stress-strain curves in three different directions ($0°, 45°$ and $90°$) with respect to the rolling direction of the plates. It was found that the steel material can be considered as isotropic with a small variation in failure strain (Figure 2a), while the aluminium alloy was slightly anisotropic both in flow stress and in elongation to failure (Figure 2b). It was also noticed that diffuse necking occurred at very small plastic strains (approximately 0.7%) in all three directions for the aluminium specimens, indicating that the elongation before necking was very low for this material. Following the argumentation in Aune et al. [28], this is due to the forming process of these sheets where the yield stress was increased by cold-working which results in reduced ductility before necking (see also Reference [31]). Moreover, a review of previous dynamic material tests of these materials showed that the steel is moderately strain-rate sensitive, while the aluminium alloy has relatively high strain-rate sensitivity [28].

2.2. Airblast experiments

A detailed presentation of the experiments is given in Aune et al. [28]. However, the experimental setup and programme are briefly repeated in the following for completeness since these experiments served as the basis for the numerical simulations.

The experimental setup is illustrated in Figure 3, where the square plate specimens with dimensions of 0.4 m x 0.4 m x 0.0008 m were clamped to a rigid mounting frame using 16

M12 bolts and a clamping frame in an attempt to achieve fixed boundary conditions. A square opening of $0.3\,\mathrm{m}\times0.3\,\mathrm{m}$ at the centre of the mounting and clamping frame defined the exposed area of the plates. The explosive mass W was positioned at various stand-off distances R relative to the centre point of the plate depending on the material. The experimental programme is given in Table 1 where each test is numbered MXY. M gives the material (S for steel and A for aluminium), X denotes the subsequent stand-off distance (1, 2 and 3) for each material and Y is the test number. The explosive material was spherical charges of Composition C-4 with a mass of 30 g (equivalent to 40.2 g of TNT) and a diameter of 34.5 mm. The blast was initiated by an electric detonator with a TNT equivalent of 1 g.

Piezoelectric pressure sensors (Kistler 603B) were used for pressure recordings. These measurements were synchronized with three-dimensional digital image correlation (3D-DIC) analyses using a stereovision setup with two high-speed cameras (Phantom v1610). This enabled a thorough investigation of the entire experiment. It should also be noted that the pressure sensors were positioned along the centre lines in the clamping frame (Figure 3), resulting in a reduced clamping of the blast-loaded plates at these locations.

Figure 4 shows measured mid-point deflection versus time from representative tests based on the 3D-DIC analyses, while the main experimental results are summarized in Table 2. All deformation profiles presented herein were corrected for the slight movement of the mounting frame. Moreover, due to trigger problems and flaking of the paint at the centre part of the plate in some tests, 3D-DIC analyses were only possible in 13 out of the 21 experiments conducted. The displacement histories reported in this study are therefore limited to the tests where 3D-DIC analyses were possible. However, the tests showed good repeatability and the reported results are considered to be a good representation of the experimental observations. It is referred to Aune et al. [28] for a more detailed presentation of the experiments and results.

3. Material model

3.1. Constitutive relation

The extreme loading conditions during blast events may involve large strains, high strain rates, temperature softening and ductile failure in metal structures. To account for these effects, an elastic-thermoviscoplastic constitutive model is used. The chosen model is similar to the computational model proposed by Børvik et al. [32] and based on the well-known Johnson-Cook constitutive relation. As a part of this work the computational model was implemented as the *VPJC* material model in EPX [30], allowing for finite strains and finite rotations. A brief presentation of the model is provided in the following.

Assuming negligible elastic strains compared to the plastic strains, a hypoelastic formulation is adopted for large deformations through an additive decomposition of the rate-of-deformation tensor

$$\mathbf{D} = \mathbf{D}^e + \mathbf{D}^p \tag{1}$$

where $\mathbf{D}^e$ and $\mathbf{D}^p$ are the elastic and plastic parts, respectively. The elastic part is defined as

$$\mathbf{D}^e = \frac{1+\nu}{E}\boldsymbol{\sigma}^{\nabla J} - \frac{\nu}{E}\mathrm{tr}\left(\boldsymbol{\sigma}^{\nabla J}\right)\mathbf{I} \tag{2}$$

where ν and E are elastic constants, $\boldsymbol{\sigma}^{\nabla J}$ is the Jaumann rate of the Cauchy stress tensor $\boldsymbol{\sigma}$ and $\mathbf{I}$ is the second order identity tensor.

The yield function is defined as

$$f(\boldsymbol{\sigma}, p, T) = \sigma_{eq}(\boldsymbol{\sigma}) - \sigma_y(p, T) \tag{3}$$

where p is the equivalent plastic strain, and T is the absolute temperature. Assuming isotropic behaviour and no kinematic hardening, the J_2 flow theory for pressure insensitive materials is adopted and the equivalent stress is expressed as

$$\sigma_{eq}(\boldsymbol{\sigma}) = \sqrt{\frac{3}{2}\boldsymbol{\sigma}' : \boldsymbol{\sigma}'} \tag{4}$$

where $\boldsymbol{\sigma}'$ is the stress deviator given as

$$\boldsymbol{\sigma}' = \boldsymbol{\sigma} - \frac{1}{3}\mathrm{tr}(\boldsymbol{\sigma})\mathbf{I} \tag{5}$$

The yield stress of the material is expressed as

$$\sigma_y(p,T) = \left[\sigma_0 + \sum_{i=1}^{2} Q_i(1-\exp(-C_i p))\right]\left[1-T^{*m}\right] \tag{6}$$

where the homologous temperature is given as $T^* = (T-T_r)/(T_m-T_r)$, T_r being the ambient temperature and T_m is the melting temperature of the material. The thermal softening is governed by the parameter m, whereas the strain hardening is described by a two-term saturation type of hardening rule proposed by Voce [33] using the yield stress σ_0 and the hardening parameters Q_1, C_1, Q_2 and C_2.

The plastic rate-of-deformation tensor is expressed through the associated flow rule as

$$\mathbf{D}^p = \dot{p}\frac{\partial f}{\partial \boldsymbol{\sigma}} = \frac{3}{2}\dot{p}\frac{\boldsymbol{\sigma}'}{\sigma_{eq}} \tag{7}$$

where the equivalent plastic strain rate $\dot{p}$ is defined as

$$\dot{p} = \begin{cases} 0 & , \ f \le 0 \\ \dot{p}_0\left(\left[\dfrac{\sigma_{eq}(\boldsymbol{\sigma})}{\sigma_y(p,T)}\right]^{\frac{1}{c}} - 1\right) & , \ f > 0 \end{cases} \tag{8}$$

Here, c is a material parameter governing the strain-rate sensitivity and $\dot{p}_0$ is a user-defined strain rate. In the viscoplastic domain ($f > 0$) the equivalent stress is found from Eq. (8) as

$$\sigma_{eq}(\boldsymbol{\sigma}) = \sigma_y(p,T)\left[1+\frac{\dot{p}}{\dot{p}_0}\right]^c = \left[\sigma_0 + \sum_{i=1}^{2} Q_i(1-\exp(-C_i p))\right]\left[1+\frac{\dot{p}}{\dot{p}_0}\right]^c\left[1-T^{*m}\right] \tag{9}$$

Since the structural response is very rapid during blast loading, adiabatic conditions may be assumed. The temperature rise is then calculated based on the plastic dissipation, i.e.,

$$\dot{T} = \frac{\chi}{\rho C_p}\boldsymbol{\sigma} : \mathbf{D}^p = \frac{\chi}{\rho C_p}\sigma_{eq}\dot{p} \tag{10}$$

where χ is the Taylor-Quinney coefficient, ρ is the density and C_p is the specific heat capacity of the material. The Taylor-Quinney coefficient represents the fraction of plastic work converted into heat, while the remaining fraction is energy stored in the material due to structural rearrangements. Typical values used in simulations are $\chi = 0$ for isothermal conditions and $\chi = 0.9$ for adiabatic conditions.

3.2. Failure criterion

Ductile failure is modelled using the Cockcroft-Latham (CL) criterion [34], which is an energy-based failure criterion using the "plastic work" per unit volume to predict failure. In this study the criterion is considered as uncoupled from the constitutive relation and reads

$$D = \frac{1}{W_c}\int_0^p \langle \sigma_1 \rangle dp = \frac{1}{W_c}\int_0^p \left\langle \sigma^* + \frac{3+\mu_\sigma}{3\sqrt{3+\mu_\sigma^2}} \right\rangle \sigma_{eq} dp \tag{11}$$

where W_c is the critical CL parameter found by integrating the major principal stress σ_1 from a uniaxial tension test over the entire equivalent plastic strain path until the plastic strain at failure p_f is reached. The Macaulay brackets imply that $\langle a \rangle = \frac{1}{2}\left(a + |a|\right)$ for any real number a and that only positive values of the major principal stress contribute to the damage evolution. Eq. (11) also shows that the CL failure criterion accounts for both the stress triaxiality σ^* and the Lode parameter μ_σ defined by

$$\sigma^* = \frac{\sigma_H}{\sigma_{eq}}, \quad \mu_\sigma = \frac{2\sigma_2 - \sigma_1 - \sigma_3}{\sigma_3 - \sigma_1} \tag{12}$$

where $\sigma_1 \geq \sigma_2 \geq \sigma_3$ are the ordered principal stresses and $\sigma_H = (\sigma_1 + \sigma_2 + \sigma_3)/3$ is the hydrostatic stress. Thus, damage is driven by plastic dissipation and amplified by a factor depending on the stress state through the parameters σ^* and μ_σ.

Material failure emerges when the damage parameter D in Eq. (11) reaches unity. This failure criterion is attractive in structural design, since only one damage parameter obtained from a single uniaxial tension test is required for calibration. Previous studies in terminal ballistics [35][36][37] have proven the robustness of the CL criterion. The dependence of both deviatoric and hydrostatic stress states were discussed by Holmen et al. [38][39], where it was shown that damage will not evolve for sufficiently low values of stress triaxiality. Moreover, experimental studies by Langdon et al. [40] on blast-loaded steel and aluminium plates indicated that the failure of ductile plates could be related to the specific energy giving tensile failure, and that failure under such conditions could be predicted from simple quasi-static tension tests.

3.3. Identification of material parameters

The material parameters σ_0, $Q_{i=1,2}$ and $C_{i=1,2}$ were identified by Aune et al. [28] and Holmen et al. [38] for the aluminium and steel materials, respectively. Both identifications were based on quasi-static material tests using inverse modelling and a similar material model (**MAT_107*) in LS-DYNA [41]. However, since these studies used a different FE software it was considered necessary to verify that the material parameters were applicable also in EPX. This further served as a validation of the implementation of the *VPJC* material model presented above.

The uniaxial tension tests presented in Section 2.1 were modelled in EPX by the same shell elements to be used in the airblast simulations, and by prescribing the same elongation

history as in the material tests. The elements were 4-node quadrilaterals (called *Q4GS*) with 6 dofs per node and 20 Gauss integration points (5 through the thickness). The entire dog-bone geometry of the specimen was modelled and the initial element size in the gauge area was equal to the thickness in an attempt to capture local necking. Mass-scaling by a factor 10^9 and 10^8 was used to speed up the computational time for the steel and aluminium specimens, respectively. Larger scaling factors resulted in non-physical inertia effects during the necking and a non-negligible kinetic energy in the simulations. Material constants for both materials are listed in Table 3, while physical constants are given in Table 4.

Comparisons between FE analyses and tensile tests are shown in Figure 2. Since necking occurred at very small strains for the aluminium alloy, results from the numerical simulations were compared to the experimental data in terms of nominal stress-strain curves. The trend in the numerical results was that the numerical models were able to describe the overall response for both materials, and that the material parameters from Aune et al. [28] were valid. Since necking occurred already at strains of approximately 0.7 % in the aluminium tests, it was necessary to include the strain-rate sensitivity term in Eq. (9) to capture the post-necking behaviour (see Figure 2b). After the initiation of necking, the strain rate increased by an order of magnitude and delayed the evolution of the neck by increasing the load-carrying capacity of the material. This was also observed in the experiments since barely any diffuse necking occurred before localized necking and failure, which may be explained by the high rate sensitivity of the material reported in the literature (see e.g. [42][43]).

The CL parameter W_c in Eq. (11) was determined based on the numerical simulations by inspecting the element exposed to the largest plastic work. This element is always located inside the neck, since localization is the first sign of material failure. The accuracy of W_c is therefore highly dependent on a proper representation of the localized necking. That is, when necking localizes in the tension test, damage will evolve rapidly in the critical element. The

W_c parameter, as obtained in this study, is therefore mesh dependent because the mesh size influences the representation of the localized necking. Only the tension tests in the rolling direction of the plate were used in the calibration, although the failure strain for the aluminium alloy was somewhat lower in the $45°$ and $90°$ directions (see Figure 2b). This also implies a spread in W_c between each material test, which (at least to some extent) may affect the numerical results. However, modelling of anisotropic failure was beyond the scope of this study. The points used to extract W_c from the numerical results are indicated by red markers in Figure 2, and the values are given in Table 3. Figure 2 shows that the numerical simulations of the steel captured the localized necking very well, while the simulation of the aluminium did not manage to predict localized necking at the same strain as in the material test. The CL parameter W_c for the aluminium alloy was therefore determined at the value of the major principal strain where failure occurred in the test.

4. Numerical simulations

4.1. Numerical model

All numerical simulations were performed in the FE software EPX [30], an explicit FE code jointly developed by the French Commissariat à l'énergie atomique et aux énergies alternatives (CEA DMT Saclay, France) and the Joint Research Centre (EC-JRC Ispra, Italy). The main application domain of the code is numerical simulations of fast transient phenomena such as explosions and impacts in complex three-dimensional fluid-structure systems.

Figure 5 illustrates the assembly of the numerical model, where the symmetry of the problem was utilized to model only one quarter of the experimental setup using symmetric boundary conditions. A mesh sensitivity study showed that an element size of 10 mm was adequate to predict the global deformation observed in the experiments. However, the plate

was modelled using a Lagrangian discretization with an element size of approximately 2.5 mm (Figure 5b) and 4-node Reissner-Mindlin shells (*Q4GS*) with 6 dofs per node and 20 Gauss integration points (5 through the thickness). The fine mesh size was chosen in an attempt to predict the tearing along the boundary observed in some of the tests using element erosion without too much loss of mass. Moreover, the material behaviour of the plates was governed by the *VPJC* model with material and physical constants from Table 3 and Table 4. Element erosion was initiated when all integration points in the element reached the critical value of the damage parameter in Eq. (11). The bolts and clamping frames were represented by 8-node brick elements (*CUB8*) with 8 Gauss points and the *VPJC* model with a high elastic limit to ensure elastic behaviour using the physical constants for steel in Table 4.

The bolted connections used in the experiments were designed with internal (female) threads in the steel mounting frame and external (male) threads on the bolts without using a traditional nut. This made it convenient to model the steel mounting frame and the bolts as one component (Figure 5a). Each bolt was pre-stressed to an initial torque ($M_t = 200$ Nm) in the tests, resulting in a clamping pressure between the frames and the plate. In the model, this was accounted for by applying an external pressure at the contact area between the bolt head and the clamping frame (see Figure 5c) while the bolts were modelled as stress-free. The contact pressure was determined using the approach suggested in Reference [44] where the pre-tensioning force $F_p = M_t / k\phi$ in each bolt was found from the applied torque M_t, bolt diameter ϕ, thread geometry and friction in the thread engagements and under the bolt heads. The thread geometry and friction were accounted for by the coefficient k, which is the main uncertainty in this approach. The recommended value for k is usually 0.18. However, according to Reference [44] it may vary between 0.10 and 0.23. The elements at the surface of the clamping frame and within the diameter of the bolt heads were defined as the contact area A_c, which was determined to be 175 mm^2. Dividing the pre-tensioning force F_p in each bolt

by this contact area resulted in a recommended contact pressure of 527 MPa between the bolt head and the clamping frame. Still, there is a large spread between the minimum and maximum values of 410 MPa and 948 MPa, respectively. This motivated a numerical study on the influence of the contact pressure on the response of the plate, which showed that the recommended value of 527 MPa gave the best agreement with the experimental observations. A contact pressure of 527 MPa was therefore used in this study. Contact between the plate, bolts and frames was modelled using a surface-to-surface contact algorithm (*GLIS*) using slave nodes and master surfaces where contact was enforced by Lagrangian multipliers when a slave node penetrated a master surface. The plate was modelled as the slave and the static friction coefficient between the plate and clamping frames was set to 0.15, while the dynamic friction coefficient was taken equal to 0.10.

4.2. Airblast loading

The positive phase of the blast load was described using the empirical parameters by Kingery and Bulmash (KB) [6] and the pressure-time history was represented by the modified Friedlander equation [9], i.e.,

$$p(t) = p_0 + p_{r\alpha}\left(1-\frac{t-t_a}{t_{d+}}\right)\exp\left(\frac{-b(t-t_a)}{t_{d+}}\right) \quad , \; t_a < t < t_a + t_{d+} \tag{13}$$

In this approach, the charge mass and stand-off distance are used as input to find the corresponding KB parameters (t_a, t_{d+}, $p_{\mathrm{so,max}}$, $p_{\mathrm{r,max}}$, i_{r+}). Then, the Friedlander equation provides the pressure-time history on each element of the plate depending on the stand-off distance and angle of incidence relative to the charge. The reflected overpressure $p_{r\alpha}$ varies as a function of the angle of incidence α between the head-on reflected overpressure $p_{\mathrm{r,max}}$ ($\alpha = 0^\circ$) and the incident (side-on) overpressure $p_{\mathrm{so,max}}$ ($\alpha = 90^\circ$). This was accounted for by

determining the reflected pressure coefficient $C_{r\alpha} = p_{r\alpha} / p_{\mathrm{so,max}}$ and oblique impulse $i_{r\alpha+}$ using the data points provided in Reference [2] and [45]. Intermediate values of the peak incident pressure $p_{\mathrm{so,max}}$ were found using linear interpolation between adjacent data points. The decay parameter b in Eq. (13) was determined using the governing parameters (i.e., $p_{r\alpha}$, $i_{r\alpha+}$, t_a, t_{d+}) integrated over the positive phase duration t_{d+}, resulting in the following implicit equation for the positive impulse

$$i_{r\alpha+} = \int_{t_a}^{t_a+t_{d+}} p_{r\alpha}\left(1-\frac{t-t_a}{t_{d+}}\right)\exp\left(\frac{-b(t-t_a)}{t_{d+}}\right) = \frac{p_{r\alpha}t_{d+}}{b^2}\left(b-1+\exp(-b)\right) \tag{14}$$

where the only unknown is b. This non-linear equation was solved iteratively to determine the value of the decay parameter b which produces the impulse $i_{r\alpha+}$.

Figure 6 shows the positive phase parameters (solid lines) as a function of scaled distance ($Z = R/W^{1/3}$), while Figure 7 presents the relevant curves used to find the reflected pressure coefficient $C_{r\alpha}$ as a function of the angle of incidence. Note that the parameters in terms of impulse and duration in Figure 6 are scaled using Hopkinson-Cranz scaling [8]. A wider range of curves for the reflected pressure coefficient can be found in References [2][45].

The negative phase was modelled using either a bilinear or a cubic representation based on the recommendations in [2] and [17][18][19], respectively. This was motivated by previous findings in References [12][21][22], suggesting that the structural response of flexible structures depends on the timing and magnitude of the peak negative pressure relative to the dynamic response. Following the recommendations in [2] and using a bilinear approximation of the negative phase, the pressure-time history for a given stand-off distance and charge mass can be given by the piecewise expression in Eq. (15), i.e.,

$$p(t)=\begin{cases} p_0 & ,\ t<t_a \\ p_0+p_{r\alpha}\left(1-\dfrac{t-t_a}{t_{d+}}\right)\exp\left(\dfrac{-b(t-t_a)}{t_{d+}}\right) & ,\ t_a<t<t_a+t_{d+} \\ p_0-p_{r,\min}\left(\dfrac{t-(t_a+t_{d+})}{0.25t_{d,\text{lin-}}}\right) & ,\ t_a+t_{d+}<t<t_a+t_{d+}+0.25t_{d,lin-} \\ p_0-p_{r,\min}\left(1-\dfrac{t-(\mathrm{t}_a+\mathrm{t}_{d+}+0.25t_{d,\text{lin-}})}{0.75t_{d,\text{lin-}}}\right) & ,\ t_a+t_{d+}+0.25t_{d-}<t<t_a+t_{d+}+t_{d,lin-} \\ p_0 & ,\ t>t_a+t_{d+}+t_{d,lin-} \end{cases} \quad (15)$$

where it is noticed that the rise time to the peak negative pressure $p_{r,\min}$ equals 1/4 of the negative phase duration $t_{d,\text{lin-}}$. Similarly, using the cubic representation of the negative phase suggested in [17][18][19], the pressure-time history may be represented by the piecewise function in Eq. (16), i.e.,

$$p(t)=\begin{cases} p_0 & ,\ t<t_a \\ p_0+p_{r\alpha}\left(1-\dfrac{t-t_a}{t_{d+}}\right)\exp\left(\dfrac{-b(t-t_a)}{t_{d+}}\right) & ,\ t_a<t<t_a+t_{d+} \\ p_0-p_{r,\min}\left(\dfrac{27}{4}\dfrac{t-(t_a+t_{d+})}{t_{d,\text{cub-}}}\right)\left(1-\dfrac{t-(t_a+t_{d+})}{t_{d,\text{cub-}}}\right)^2 & ,\ t_a+t_{d+}<t<t_a+t_{d+}+t_{d-} \\ p_0 & ,\ t>t_a+t_{d+}+t_{d-} \end{cases} \quad (16)$$

For a cubic representation it can be shown that the rise time to the peak negative pressure $p_{r,\min}$ equals 1/3 of the negative phase duration $t_{d,\text{cub-}}$. Both approximations of the negative phase are illustrated in Figure 8. The negative phase parameters were taken from Reference [2] which is in good agreement with the analytical work reported by Granström [17]. Thus, the peak negative pressure $p_{r,\min}$ and the impulse i_{r-} were calculated using empirical expressions based on curve fitting to the diagrams presented for a spherical charge in [2], i.e.,

$$p_{\mathrm{r,min}}=\begin{cases} 100 & ,\ Z<0.803 \\ 79.433\mathrm{Z}^{-1.05} & ,\ Z\geq 0.803 \end{cases} \quad \text{(kPa)} \quad (17)$$

$$i_{r-} = \begin{cases} 480 \cdot W^{1/3} & , Z < 0.608 \\ 10^{-0.87731 \cdot \log(Z) + 2.49145} \cdot W^{1/3} & , Z \geq 0.608 \end{cases} \quad \text{(kPa ms)} \tag{18}$$

$$t_{d-} = \begin{cases} (0.694 \cdot \log(Z) + 8.963) \cdot W^{1/3} & , Z < 0.255 \\ (2.305 \cdot \log(Z) + 9.918) \cdot \mathrm{W}^{1/3} & , 0.255 \leq Z \leq 3.116 \\ 11.056 \cdot W^{1/3} & , Z > 3.116 \end{cases} \quad \text{(ms)} \tag{19}$$

The negative phase parameters are shown as dashed lines in Figure 6, where the expression for the negative phase duration t_{d-} in Eq. (19) is included for completeness. The duration of the bilinear and cubic representations was found by integration of the pressure during the negative phase in Eqs. (15) and (16) so that the impulse i_{r-} from Eq. (18) is conserved, i.e.,

$$t_{d,lin-} = 2\frac{i_{r-}}{p_{r,\min}} \tag{20}$$

$$t_{d,\mathrm{cub}-} = \frac{16}{9}\frac{i_{r-}}{p_{r,\min}} \tag{21}$$

These equations were implemented in EPX as the *AIRB* directive where the user can choose the preferred negative phase representation. Note that the effect of the angle of incidence during the negative phase was assumed similar to that during the positive phase. That is, the negative impulse i_{r-} in Eq. (18) was corrected for the angle of incidence using the scaling factor $i_{r\alpha+} / i_{r+}$ found from the correction of the positive impulse. Previous studies by Rigby et al. [46] have shown that the angle of incidence has negligible effects on the negative pressure, and it was therefore considered sufficient to use the parameter given in Eq. (17) also at oblique angles of incidence.

Finally, a validation of the positive phase predicted by the *AIRB* directive was performed. This was carried out by comparing experimental measurements with numerical predictions at the sensors located in the clamping frame (see Figure 3). The validation was limited to the positive phase only, due to difficulties related to the measurements of the negative phase in

Aune et al. [28]. The results are summarized in Table 2, while typical pressure-time histories from experiments are compared to numerical results in Figure 9. It should be noted that the experimental tests are only denoted by their material and stand-off distance (i.e., S1, S2, S3, A0, A1, A2 and A3) in the following. Moreover, the experimental data were low-pass filtered with a cut-off frequency of 0.05 times the sampling rate (10 MHz). Figure 9 shows good agreement between experimental and numerical results, and Table 2 shows that the peak reflected overpressure $p_{r\alpha}$ and the positive impulse $i_{r\alpha+}$ are in reasonable correspondence with the experimental values. However, the predicted positive duration t_{d+} from the *AIRB* directive was found to be significantly longer than that reported in the experiments. This is due to a rather long tail of the pressure history where the corresponding magnitudes were negligible (see Figure 9). Thus, the pressure-time histories were in close agreement with the pressure levels contributing to the structural response. This is also confirmed by the good agreement between experiments and numerical results in terms of peak reflected pressures and impulses. It is also emphasized that when considering only the positive phase of the blast loading these experiments were in the impulsive loading domain due to the short duration compared to the natural period of vibration of the plates [28]. The response to such short pulses is essentially independent of the pulse shape and the magnitude of the impulse is the parameter governing the structural response. Hence, the *AIRB* directive was found to be able to predict the positive phase of the blast loading.

4.3. Parametric study

Before simulating all the experiments in Table 1 it was decided to perform a parametric study on the negative phase representation since the recommendations in the literature are somewhat contradictory. The study was performed on plates experiencing CIB due to RSB (i.e., tests S3 and A3). The timing of the peak negative pressure was studied using both

bilinear and cubic negative phase representations, because they used the same magnitude of impulse and peak negative pressure (Figure 8). The influence of the boundary conditions was also studied since some sliding at the supports occurred in the experiments due to the reduced clamping at the pressure sensors. The model presented in Section 4.1 (hereafter denoted the "contact model") was therefore compared to a simplified model (called the "fixed model") where all nodes located between the mounting and clamping frames were fully fixed against translation in all directions. Figure 10 summarizes the results in terms of mid-point deflection versus time, while deformation profiles at maximum and minimum deflection are presented in Figure 11. Solid and dashed lines are related to the representation of the negative phase. That is, solid lines are the mid-point deflection when the negative phase was represented as bilinear, while dashed lines are from simulations with a cubic representation of the negative phase. Cyan and blue lines represent the simulations considering only the positive phase of the loading for the contact and fixed model, respectively.

In general, the parametric study showed that CIB was dependent on the timing and magnitude of the peak negative pressure relative to the dynamic response of the plates. In most of the cases, CIB was not predicted without including the negative phase of the blast loading. Moreover, as in the experiments, two distinctive types of CIB were identified. CIB of type I was driven by elastic effects during the rebound after peak deflection in the intuitive direction (i.e., the positive direction in Figure 10a). This type of CIB occurred in the S3 tests and was dependent on the axial restraint at the boundary where the elastic rebound was enhanced by the negative phase which occurred during the rebound itself. However, CIB was also observed in the simulation with only positive phase loading and fixed boundary conditions. This resulted in rather large oscillations around the final equilibrium configuration (blue line in Figure 10a). In general, the contact model including the negative phase of the loading resulted in the best agreement with the experimental observations. It was also evident

that for CIB of type I observed in the S3 tests, the effect of including the negative phase was more significant than the chosen representation (bilinear versus cubic in Figure 10a).

The A3 tests experienced another type of CIB which is referred to as type II. This type of CIB also occurred due to the negative phase, but during the oscillations following the elastic rebound (Figure 10b). CIB of type II was highly dependent on the timing of the peak negative pressure relative to the oscillations around the permanent equilibrium state of the plate. Since this is an unstable configuration, sensitive to small changes in loading and structural conditions, the timing of the negative phase may result in significant enhancement of the elastic oscillations subsequent to the elastic rebound. It was also observed that the cubic representation of the negative phase resulted in somewhat earlier RSB compared to the bilinear representation. This makes it reasonable to assume that the initial pressure gradient of the negative phase is important in determining the timing of RSB, since the initial pressure gradient was significantly steeper in the cubic representation (see Figure 8 and Figure 10).

With one exception, the general trend was that RSB is not predicted without including the negative phase of the blast loading. By investigating the deformation profiles at maximum and minimum permanent deflection in Figure 11, it was observed that the local dent occurring at the centre of the plates in the experiments was only captured in the numerical simulations with the contact model. It should be emphasized that this dent made the comparison of the mid-point deflections in Figure 10 somewhat misleading since the dent was not captured when using the fixed model (Figure 11b and Figure 11d). Thus, modelling the contact boundary conditions and including the negative phase resulted in the best agreement with the experimental data. As expected, the deformation profiles at maximum deflection in Figure 11a and Figure 11c were only dependent on the boundary conditions because the maximum deformation occurred before the negative phase. Thus, the deformation profiles of the bilinear

and cubic representation of the negative phase coincided since the deformation was unaltered by the negative pressure at this point in time.

4.4. Numerical simulations of blast-loaded plates

Based on the parametric study it was decided to use the assembly presented in Figure 5 and to follow the recommendations in Reference [2] with a bilinear representation of the negative phase when simulating all the tests on blast-loaded plates in Table 1. The numerical results are summarized and compared to the experimental data in terms of mid-point deflection versus time in Figure 12, while the maximum mid-point deflection $d_{z,\max}$ is compared to the experimental data in Table 2. A comparison of the experimental and numerical test configurations experiencing failure is presented in Figure 13. The total positive and negative impulses transmitted to the blast-loaded plates and the corresponding maximum deflection-thickness ratios obtained from the numerical simulations are reported in Table 5. This may be valuable information when discussing these experiments and findings in view of similar impulsively loaded plates reported in the literature (see e.g. [47][48]).

It is observed that the numerical simulations were in good agreement with the experimental observations, and the numerical model was able to predict the entire range of structural response from RSB at the largest stand-off distances (Figure 12) to tearing along the boundary (Figure 13). However, the oscillations subsequent to the elastic rebound were somewhat overestimated in the numerical simulations of the A1 tests compared with the experiments. This was probably due to a slightly overestimated width of the crack, resulting in reduced stiffness during the negative loading phase. Failure cannot occur in less than one element size when using element erosion and a better prediction of the crack propagation would require a refined mesh. It is emphasized that W_c is mesh size dependent when determined from inverse modelling and the same element size should be used in both

simulation and calibration. Larger elements may diffuse the failure process and suppress the crack propagation [49]. This was not feasible in this study since a mesh size of 0.8 mm was necessary to capture the localized necking in the material tests (see Section 3.3). Thus, the computational costs in the evaluation of the blast-loaded plates would be very high with such a fine mesh. However, a separate analysis of the A1 configuration with the same mesh size as that used in the calibration of W_c was performed to evaluate the influence of mesh size on the crack propagation. This resulted in complete tearing along the boundary, while the global response until failure remained the same. The W_c parameter in Table 3 should therefore be treated with some caution. Still, the numerical simulations using an element size of 2.5 mm captured the failure observed in the experiments well using a rather simple material model. This also indicated that the modelling of reduced clamping in the vicinity of the pressure sensors is an important aspect in predicting the failure observed in the experiments (Figure 3 and Figure 5). Due to the reduced clamping, failure was first observed at the bolts closest to the centre of the plate boundary (Figure 13c-d). The distinct inward deflection of the plates at the boundary was also captured in the numerical simulations experiencing failure. This is sometimes called the pulling-in effect [50] and is a result of the plate deformation which continues between the time of first tearing at the boundary (Figure 13c-d) and complete tearing at the corners (Figure 13a-b). A more detailed investigation of the failure process is beyond the scope of this study.

Since the numerical model was able to predict the experimental response with good accuracy, a numerical investigation was performed on which combinations of stand-off distance R and plate thickness t resulted in CIB due to RSB. All stand-off distances within the domain $R \in [0.525, 1.000]$ m and $R \in [0.275, 0.775]$ m for the aluminium and steel plates, respectively, were simulated in combination with thicknesses in the range $t \in [0.2, 3.6]$ mm and $t \in [0.2, 2.2]$ mm. The results are shown in terms of response spectra of the permanent

mid-point deflection in Figure 14, while mid-point deflection versus time for some typical thicknesses and stand-off distances are shown in Figure 15. The grey markers in Figure 14 illustrate the combination of stand-off distance and plate thickness used in the numerical simulations to generate the response spectra. Keep in mind that the discussion in the following is limited to these particular domains. Also recall that CIB is characterized by a permanent deflection in the opposite direction to the incident blast wave. This implies a negative permanent mid-point deflection which is indicated by a blue colour in Figure 14 and Figure 15. Similarly, a red colour indicates a permanent deflection in the same direction as the incoming blast wave, while a green colour indicates a final configuration with negligible mid-point deflection.

The numerical investigation observed both types of CIB (either type I during or type II subsequent to the elastic rebound) within a narrow range of stand-off distances and plate thicknesses for both materials. Thus, the study confirms that CIB is a response which occurs within a limited range of loading and structural conditions, and that this behaviour is related to thin flexible structures. In particular, the results indicated that CIB Type I is related to the starting time of the negative phase t_{d+} relative to the elastic rebound after maximum deflection, while CIB Type II may occur at small thicknesses when the ratio between the positive and negative impulses approaches the same order of magnitude. The simulations also provide some other interesting results, such as failure at the centre of the plate and complete tearing at the boundary during RSB for the smallest thicknesses (see Figure 15). In the simulations experiencing failure, the mid-point deflection at the point of complete failure was used in the response spectra. This indicates that although the ultimate deflection is most often used as a design criterion since this is related to the maximum stress state, damage accumulates during RSB and thin plates may fail during reversed motion. The different types of CIB were characterized by a transition zone where the turning point seemed to be at a

thickness $t = 0.6$ mm for the steel plates (Figure 14a) and $t = 1.0$ mm for the aluminium plates (Figure 14b). That is, type II CIB occurred in the dark blue area at thicknesses smaller than 0.6 mm for the steel plates, and in the dark blue area at thicknesses smaller than 1.0 mm for the aluminium plates. CIB of type I and II are indicated by solid and dashed blue lines, respectively, in Figure 15b and Figure 15d. As expected, increased stand-off distance and plate thickness resulted in oscillations approaching the initial configuration of zero mid-point deflection (a green colour in Figure 14 and Figure 15).

The findings in this study therefore broaden the range of loading properties resulting in RSB, because previous studies (see e.g. [23][24][25]) mainly consider projectile impacts or positive pulses as the loading. In such environments there is no negative phase loading and the CIB is driven by the ratio between the bending and membrane energy (i.e., the maximum deflection and the corresponding rotation in the plastic hinges at which reverse motion starts). This is further argued by the fact that the response is membrane dominated due to the large deflection-thickness ratios observed in these experiments (see Table 5). Jones [47] showed that the bending contributions are negligible compared to the membrane forces for plated structures experiencing a deflection-thickness ratio larger than one.

5. Concluding remarks

A numerical model in EUROPLEXUS (EPX) has been validated against experimental data in predicting the inelastic response of thin aluminium and steel plates exposed to blast loading. Such investigations are important in the development of advanced computational methods used in protective design. The numerical results were generally in good agreement with the experimental data and covered the entire range of inelastic response. This included partial and complete tearing along the boundaries at the closest stand-off distances and a counter-intuitive behaviour (CIB) where the permanent deflection of the plate was in the

opposite direction to the incoming blast wave due to reversed snap buckling (RSB). The influence of elastic effects and negative phase on RSB was studied numerically, and two types of CIB were identified within a narrow range of loading and structural conditions. Both types of CIB were found to depend on the timing and magnitude of the peak negative pressure relative to the dynamic response of the structure. In particular, CIB of type I was driven by elastic effects enhanced by the negative phase during the elastic rebound, while type II occurred during the subsequent oscillations after the elastic rebound and was related to the timing of the peak negative pressure and the ratio between positive and negative impulses. The plate thickness and material were found to be governing structural properties, where plate thicknesses less than about 1.6 mm and 3.2 mm may result in CIB for the steel and aluminium material, respectively. The influence of the material was evident by comparing steel and aluminium plates at the same stand-off distance ($R = 0.375$ m), which resulted in a completely different structural response since the steel plates experienced RSB whereas the permanent displacement of the aluminium plates was in the intuitive direction.

It is also emphasized that the characteristic loading domain is often determined based on the duration of the positive phase relative to the natural period of the structure (see e.g. [51]). The loading domain will then determine the computational method to be used in the blast-resistant design. Following this classification, the experiments presented herein fall into the impulsive loading domain where the blast load has vanished before the structure undergoes any significant deformation. Consequently, the response is assumed to depend only on the magnitude of the positive impulse and not on the evolution of the pressure-time history. This study shows that the blast-loaded plates experienced severe blast-structure interaction effects during the negative phase. Thus, the loading domain of thin plates and flexible structures should not be determined solely based on the positive phase of the blast load. In particular, if the timing of the negative phase is such that it will enhance elastic oscillations during (CIB

type I) or subsequent (CIB type II) to the elastic rebound, thin plates cannot be categorized into the impulsive loading domain since the negative phase may dominate the response. Finally, previous studies have suggested that the negative phase can be ignored at scaled distances with relatively small magnitudes in peak negative pressure $p_{r,min}$ compared to the peak reflected overpressure $p_{r\alpha}$ (e.g. [12]). However, the observations in this study extend the range of applications where the negative phase should be considered, because CIB was observed at relatively large peak reflected overpressures. This implies that the relative pressure magnitudes are not the only important parameter of the loading, but also the ratio between the specific positive and negative impulses could be used as an indication for CIB. In particular, it is found that RSB (i.e., CIB type II) may dominate the response of thin aluminium and steel plates when the positive and negative impulses are of the same order of magnitude.

Acknowledgement

The present work has been carried out with financial support from the Structural Impact Laboratory (SIMLab), Centre for Research-based Innovation (CRI), at the Norwegian University of Science and Technology (NTNU), and the Institute for the Protection and Security of the Citizen at the Joint Research Centre (EC-JRC).

References

[1] D. Hyde, ConWep – Application of TM 5-855-1. Fundamentals of Protective Design for Conventional Weapons. Structural Mechanics Division, Structures Laboratory, USACE Waterways Experiment Station, Vicksburg, MS, USA (1992).

[2] US Army Corps of Engineers, Naval Facilities Engineering Command, Air Force Civil Engineer Support Agency. Structures to resist the effects of accidental explosions. UFC 3-340-02. Supersedes TM5-1300, dated November 1990. US Department of Defense, Washington, DC, December 2008.

[3] Z. Xue, J. W. Hutchinson. Preliminary assessment of sandwich plates subjected to blast. International Journal of Mechanical Science 2003;45:687-705.

[4] V. Aune, E. Fagerholt, M. Langseth, T. Børvik. A shock tube facility to generate blast loading on structures. International Journal of Protective Structures 2016. Article in Press. DOI: 10.1177/2041419616666236.

[5] R. Rajendran, J. M. Lee. Blast loaded plates. Marine Structures 2009; 22: 99-129.

[6] C. N. Kingery, G. Bulmash. Airblast Parameters from TNT Spherical Air Burst and Hemispherical Surface Burst. Defence Technical Information Center, Ballistic Research Laboratory, Aberdeen Proving Ground, Maryland, 1984.

[7] G. F. Kinney, K. J. Graham. Explosive shocks in air. Springer, Berlin, 1985.

[8] W. E. Baker, P. S. Westine, F. T. Dodge. Similarity Methods in Engineering Dynamics: Theory and Practice of Scale Modeling. Elsevier Science Publishers B.V., Amsterdam, Netherlands, Revised Edition, 1991.

[9] F. G. Friedlander. The diffraction of sound pulses. I. Diffraction by a semi-infinite plane. Proceedings of the Royal Society A: Mathematical, Physical and Engineering Science, 1946;186(1006):322-344.

[10] M. Larcher. Simulation of the effects of an air blast wave. JRC Technical Report, EUR 41337EN, Luxembourg, 2007.

[11] V. Karlos, G. Solomos, M. Larcher. Analysis of the blast wave decay coefficient using the Kingery-Bulmash data. International Journal of Protective Structures 2016. Article in Press. DOI: 10.1177/2041419616659572.

[12] T. Krauthammer, A. Altenberg. Negative phase blast effects in glass panels. International Journal of Impact Engineering 2000;24(1):1-17.

[13] M. Larcher, G. Solomos, F. Casadei, N. Gebbeken. Experimental and numerical investigations of laminated glass subjected to blast loading. International Journal of Impact Engineering 2012;39:42-50.

[14] C. Gantes, N. Pnevmatikos. Elastic-plastic response spectra for exponential blast loading. International Journal of Impact Engineering 2004;30(3):323-343.

[15] J. Wei, L. R. Dharani. Response of laminated architectural glazing subjected to blast loading. International Journal of Impact Engineering 2006;32(12):2032-2047.

[16] M. Teich, N. Gebbeken. The influence of the underpressure phase on the dynamic response of structures subjected to blast loads. International Journal of Protective Structures 2010;1(2):219-233.

[17] S. A. Granström. Loading characteristics of air blasts from detonating charges. Technical Report 100, Transactions of the Royal Institute of Technology, Stockholm, 1956.

[18] Naval Facilities Engineering Command. Blast Resistant Structures. Alexandria, VA, DM 2.08, 1986.

[19] US Army Corps of Engineers. Methodology manual for the Single-Degree-of-Freedom Blast Effects Design Spreadsheets (SBEDS). ACE Protective Design Centre, USA, PDC TR-06-01 Rev 1, September 2008.

[20] S. E. Rigby, A. Tyas, T. Bennett, S. D. Clarke, S. D. Fay. The negative phase of the blast load. International Journal of Protective Structures 2014;5(1):1-20.

[21] L. M. Bryant, J. M. Erekson, K. W. Herrle. Are You Positive About Negative Phase?. In: American Society of Civil Engineers (ASCE) Structures Congress 2013:103-114.

[22] S. U. Galiev. Experimental observations and discussion of counterintuitive behavior of plates and shallow shells subjected to blast loading. International Journal of Impact Engineering 1996;18:783-802.

[23] T. X. Yu. Chapter 9: Elastic effects in the dynamic plastic response of structures, Structural Crashworthiness and failure. In: Proceedings of the Third International Symposium on Structural Crashworthiness, Edited by N. Jones and T. Wierzbicki, Taylor & Francis Ltd 1993:295-332.

[24] Q. M. Li, L. M. Zhao, G. T. Yang. Experimental results on the counter-intuitive behaviour of thin clamped beams subjected to projectile impact. International Journal of Impact Engineering 1991;11:341-348.

[25] P. S. Symonds, T. X. Yu. Counterintuitive behavior in a problem of elastic-plastic beam dynamics. ASME Journal of Applied Mechanics 1985;52:517-522.

[26] Q. M. Li, Y. M. Liu, G. W. Ma. The anomalous region of elastic-plastic beam dynamics. International Journal of Impact Engineering 2006;32:1357-1369.

[27] E. A. Flores-Johnson, Q. M. Li. A brief note on the counter-intuitive region of a square plate. International Journal of Impact Engineering 2011;38:136-138.

[28] V. Aune, E. Fagerholt, K. O. Hauge, M. Langseth, T. Børvik. Experimental study on the response of thin aluminium and steel plates subjected to airblast loading. International Journal of Impact Engineering 2016;90:106-121.

[29] F. Casadei, J. P. Halleux, A. Sala, F. Chillè. Transient fluid-structure interaction algorithms for large industrial applications. Computer Methods in Applied Mechanics and Engineering 2001;190:3081-3110.

[30] EUROPLEXUS user's manual, Joint Research Centre. http://europlexus.jrc.ec.europa.eu/public/ manual_pdf/manual.pdf [accessed 10.08.2016].

[31] European Committee for Standardization (CEN). NS-EN 515, Aluminium and aluminium alloys – Wrought products – Temper designations; 1993.

[32] T. Børvik, O. S. Hopperstad, T. Berstad, M. Langseth. A computational model of viscoplasticity and ductile damage for impact and penetration. European Journal of Mechanics A/Solids 2001;20:685-712.

[33] E. Voce. The relationship between stress and strain for homogenous deformation. Journal of the Institute of Metals 1948;74:536-562.

[34] M. G. Cockcroft, D. J. Latham. Ductility and the workability of metals. Journal of the Institute of Metals 1968;96:33-39.

[35] S. Dey, T. Børvik, O. S. Hopperstad, M. Langseth. On the influence of fracture criterion in projectile impact of steel plates. Computational Materials Science 2006;38:176-191.

[36] T. Børvik, S. Dey, A. H. Claussen. Perforation resistance of five different high-strength plates subjected to small-arms projectiles. International Journal of Impact Engineering 2009;36:948-964.

[37] A. Kane, T. Børvik, A. Benallal, O. S. Hopperstad. Failure criteria with unilateral conditions for simulation of plate perforation. European Journal of Mechanics – A/Solids 2011;30:468-476.

[38] J. K. Holmen, O. S. Hopperstad, T. Børvik. Low velocity impact on multi-layered dual-phase steel plates. International Journal of Impact Engineering 2015;78:161-177.

[39] J. K. Holmen, J. Johnsen, O. S. Hopperstad, T. Børvik. Influence of fragmentation on the capacity of aluminium alloy plates subjected to ballistic impact. European Journal of Mechanics A/Solids 2016;55:221-233.

[40] G. S. Langdon, W. C. Lee, L. A. Louca. The influence of material type on the response of plates to air-blast loading. International Journal of Impact Engineering 2015;78:150-160.

[41] Livermore Software Technology Corporation (LSTC). http://www.lstc.com [accessed 11.08.16].

[42] J. D. Campbell. Dynamic plasticity: macroscopic and microscopic aspects. Material Science and Engineering 1973;12:3-21.

[43] N. Jones. The credibility of predictions for structural designs subjected to large dynamic loadings causing inelastic behaviour. International Journal of Impact Engineering 2013;53:106-114.

[44] European Committee for Standardization (CEN). NS-EN 1090-2:2008+A1:2011, Execution of steel structures and aluminium structures - Part 2: Technical requirements for steel structures; 2008.

[45] U.S. Army Material Command. Engineering design handbook. Explosions in air. Part one. AD/A-003 817, Alexandria, Virginia, 1974.

[46] S. E. Rigby, S. Fay, A. Tyas, J. Warren, S. Clarke. Angle of incidence effects on far-field positive and negative phase blast parameters. International Journal of Protective Structures 2015;6(1):23-42.

[47] N. Jones. Structural Impact. 2nd edition, Cambridge University Press, 2012.

[48] S. Chung Kim Yuen, G. N. Nurick, G. S. Langdon, Y. Iyer. Deformation of thin plates subjected to impulsive load: Part III – an update 25 years on. International Journal of Impact Engineering 2016. Article in Press. DOI:10.1016/j.ijimpeng.2016.06.010.

[49] C. Ruggieri, T. L. Panontin, R. H. Dodds Jr. Numerical modelling of ductile crack growth in 3-D using computational cell elements. International Journal of Fracture 1996;82:67-95

[50] G. N. Nurick, G. C. Shave. The deformation and tearing of thin square plates subjected to impulsive loads – An experimental study. International Journal of Impact Engineering 1996;18(1):99-116.

[51] D. Dusenberry. Handbook of Blast-Resistant Design of Buildings. John Wiley & Sons, 2010.

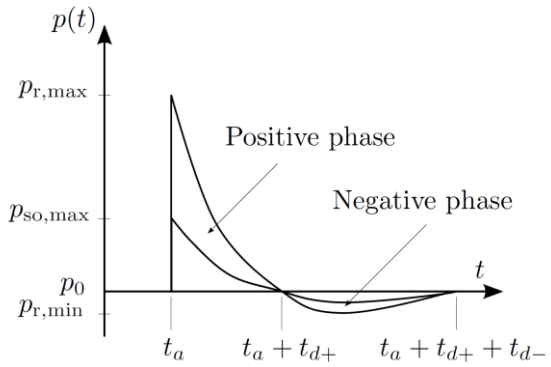

Figure 1. Typical pressure-time history for a blast wave.

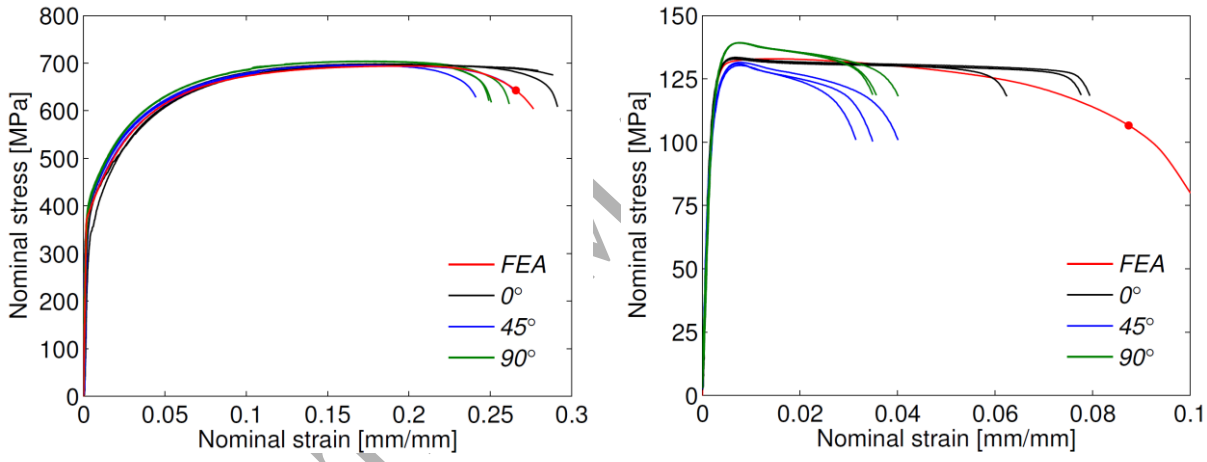

(a) Steel (b) Aluminium

Figure 2. Nominal stress-strain curves from uniaxial tensile tests along three different loading directions for (a) Docol 600DL and (b) EN AW 1050A-H14. Numerical results from EPX (FEA) with material data from Table 3 and Table 4 are included for comparison. The red dots denote the point of failure in the calculation of W_c.

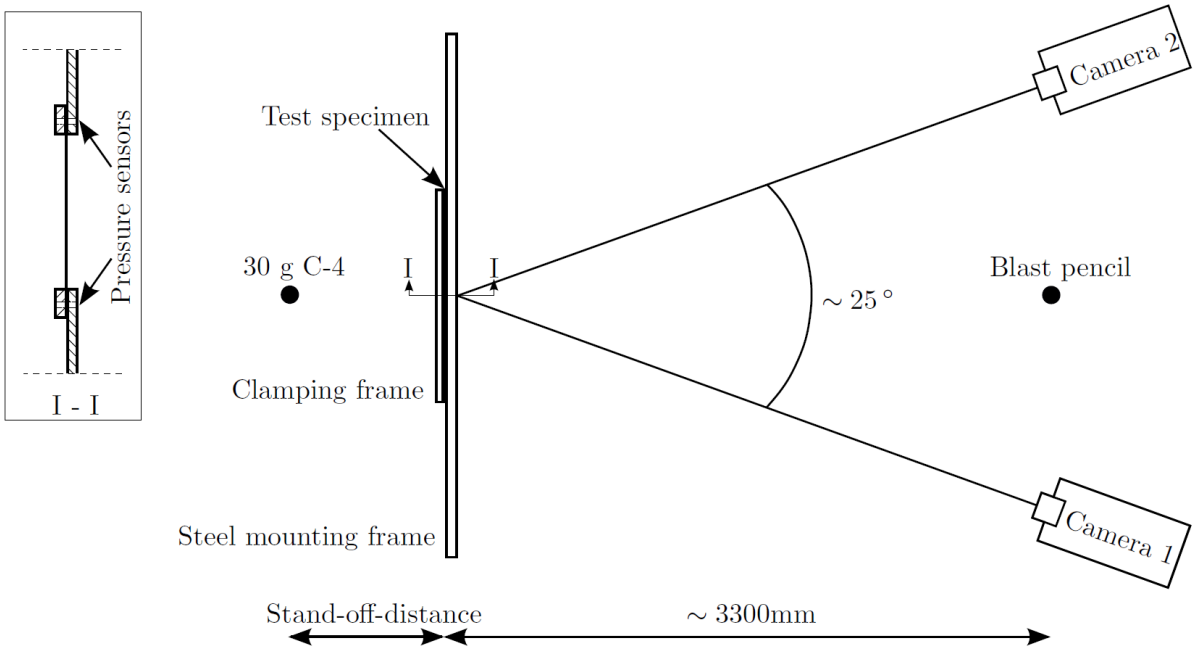

Figure 3. Sketch of experimental setup used by Aune et al. [28].

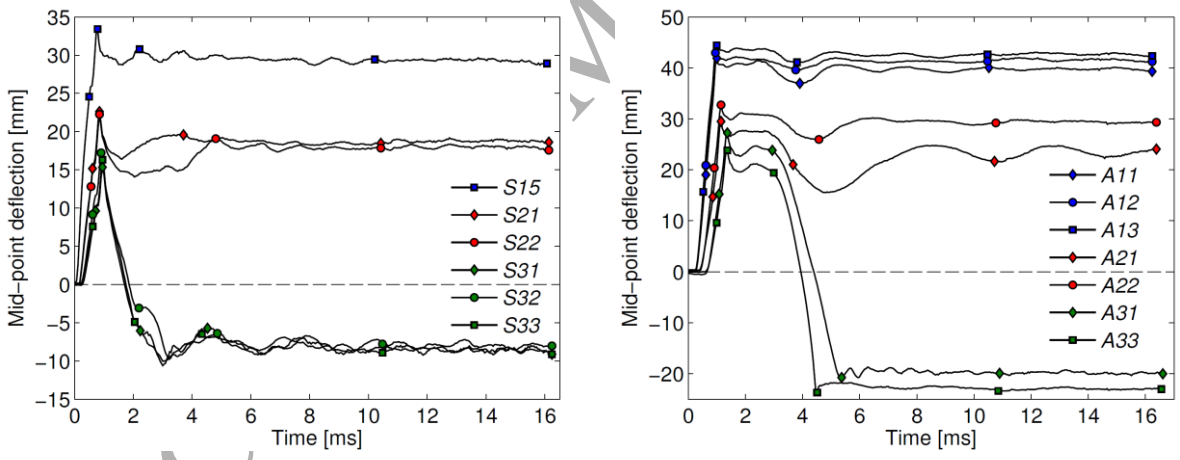

(a) Steel plates (b) Aluminium plates

Figure 4. Mid-point deflection of the plates based on 3D-DIC measurements. All curves are corrected for the movement of the mounting frame.

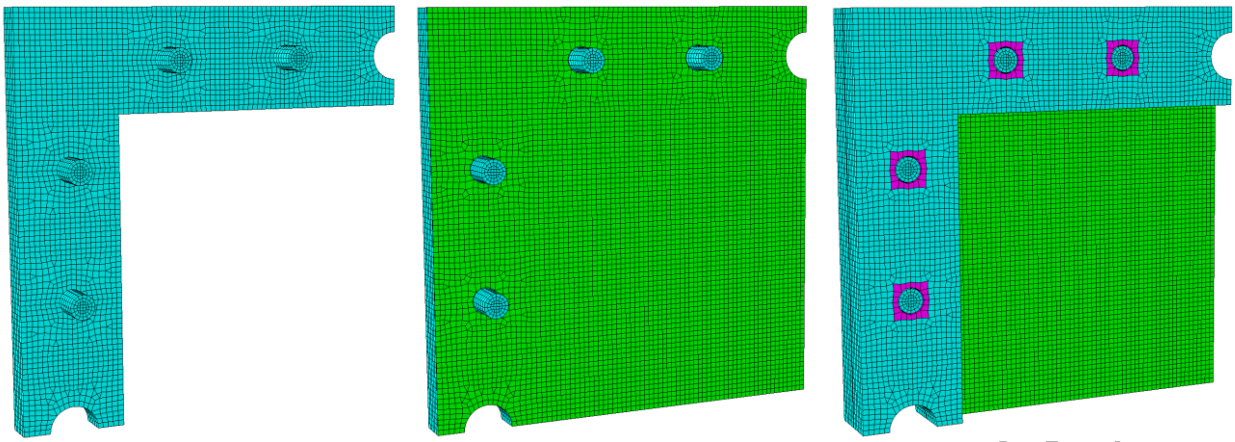

(a) (b) (c)

Figure 5. Numerical model showing (a) steel mounting frame and bolts as one component (in cyan), (b) plate specimen (in green) and (c) complete assembly including the clamping frame (also in cyan) and contact area between bolt heads and clamping frame (in magenta) used to model the effect of the pre-tensioning of the bolts.

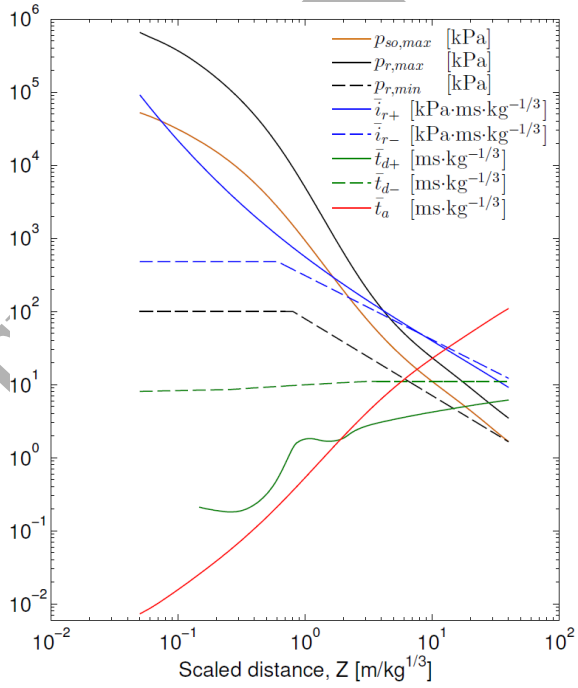

Figure 6. Positive and negative phase parameters of the reflected blast wave from a spherical charge of TNT detonated in free air. The positive phase parameters in [2][6] are plotted with solid lines, while the negative phase parameters are shown with dashed lines.

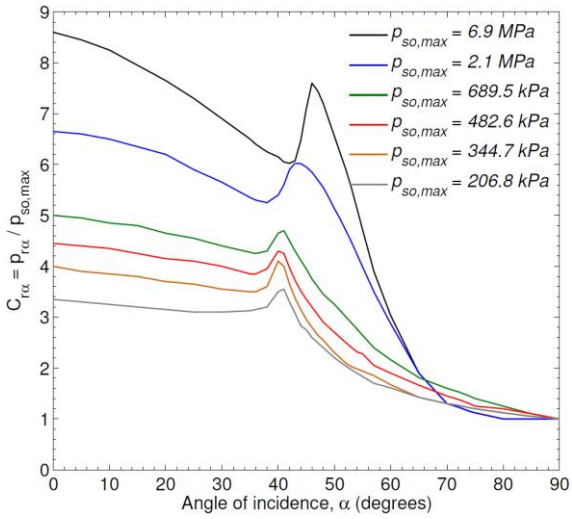

Figure 7. Reflected pressure coefficient versus angle of incidence [2][45]. The angle of incidence is defined as the angle between the normal vector and the direct vector between the charge and the point of interest on the target.

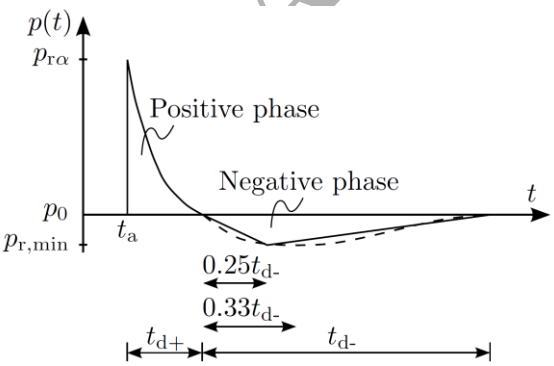

Figure 8. Pressure-time history with either bilinear (solid line) or cubic (dashed line) representation of the negative phase.

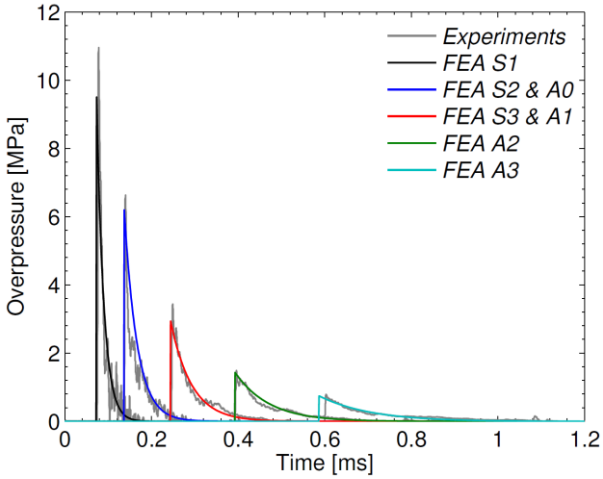

Figure 9. Comparison between experimental and numerical pressure recordings during the positive phase. The numerical results are taken from the clamping frame for comparison with the experimental data from Aune et al. [28].

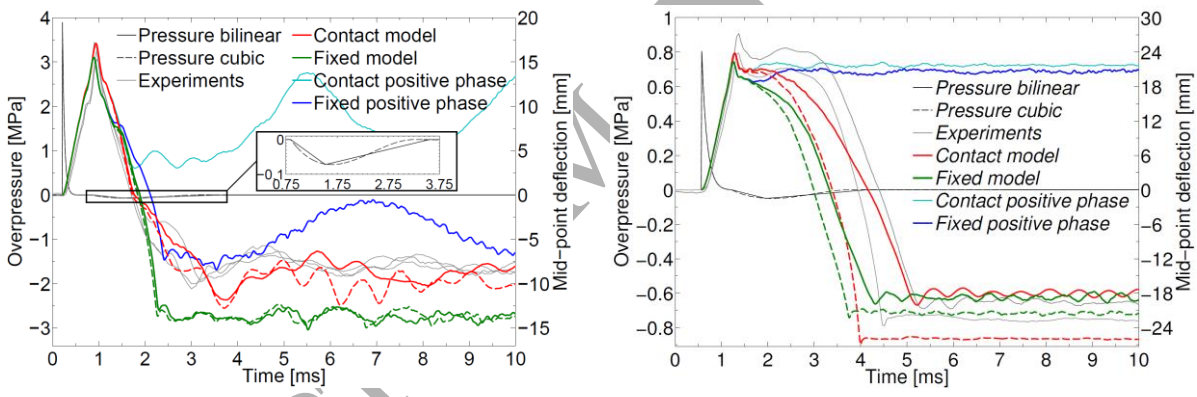

(a) S3 (b) A3

Figure 10. Results from parametric studies on tests S3 and A3. Both pressure and deflection were taken from the centre of the plates. Solid lines correspond to a bilinear representation of the negative phase, while dashed lines indicate a cubic representation. Cyan and blue lines represent only positive phase loading for the contact and fixed model, respectively.

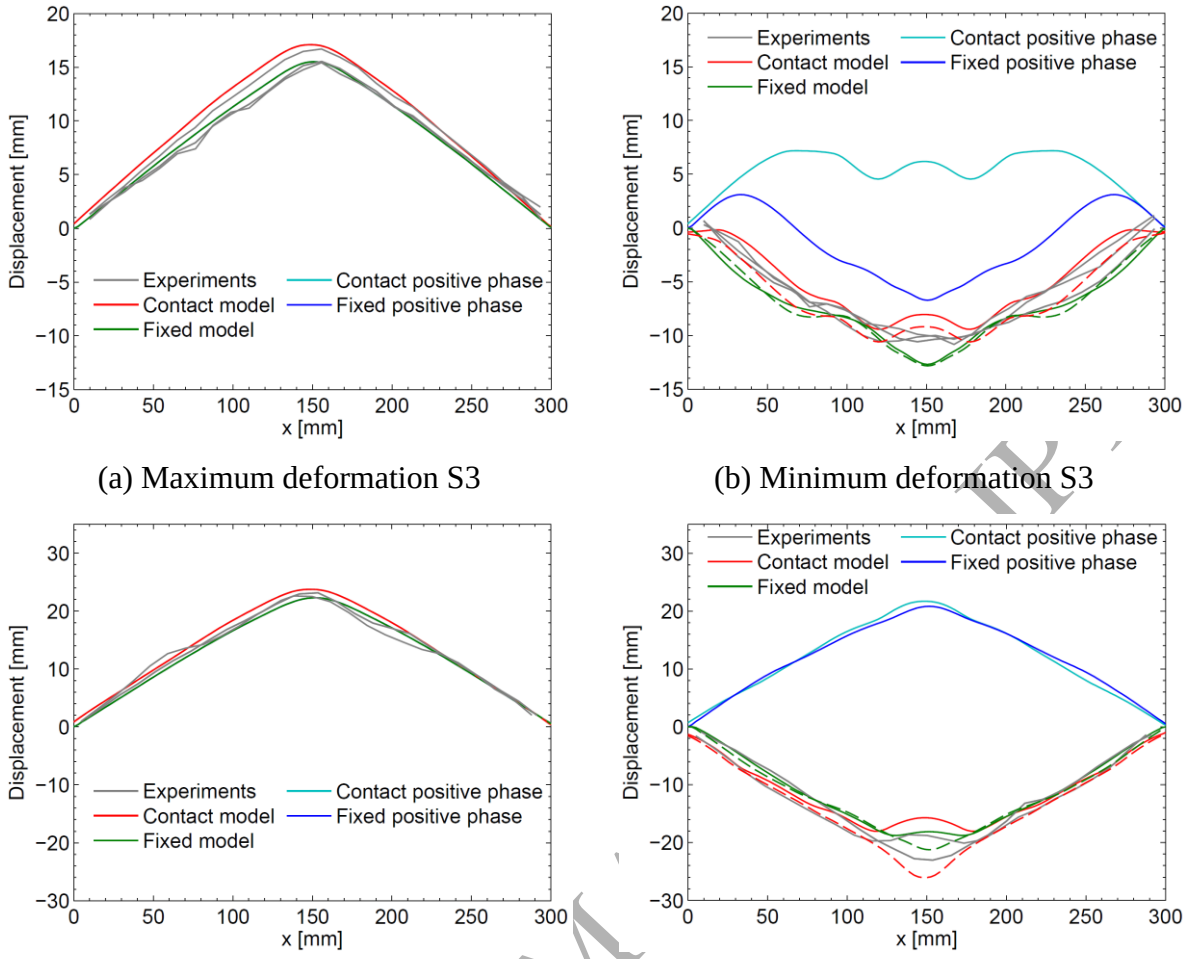

(a) Maximum deformation S3

(b) Minimum deformation S3

(c) Maximum deformation A3

(d) Minimum deflection A3

Figure 11. Comparison of deformation profiles at maximum and minimum mid-point deflection when varying the negative phase representation and boundary conditions. Solid lines correspond to a bilinear representation of the negative phase, while dashed lines indicate a cubic representation. Cyan and blue lines represent only positive phase loading for the contact and fixed model, respectively.

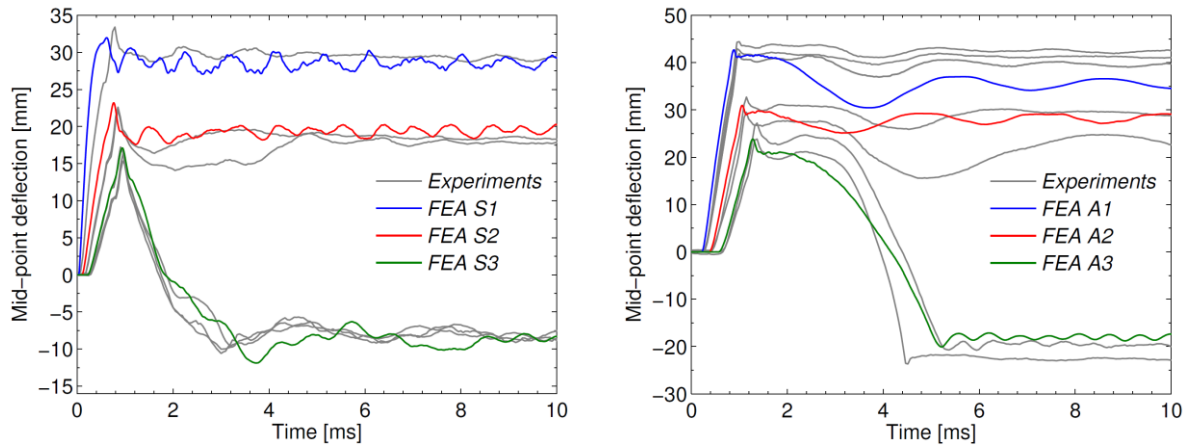

(a) Steel plates

(b) Aluminium plates

Figure 12. Comparison of numerical (FEA) and experimental results in terms of mid-point deflection histories.

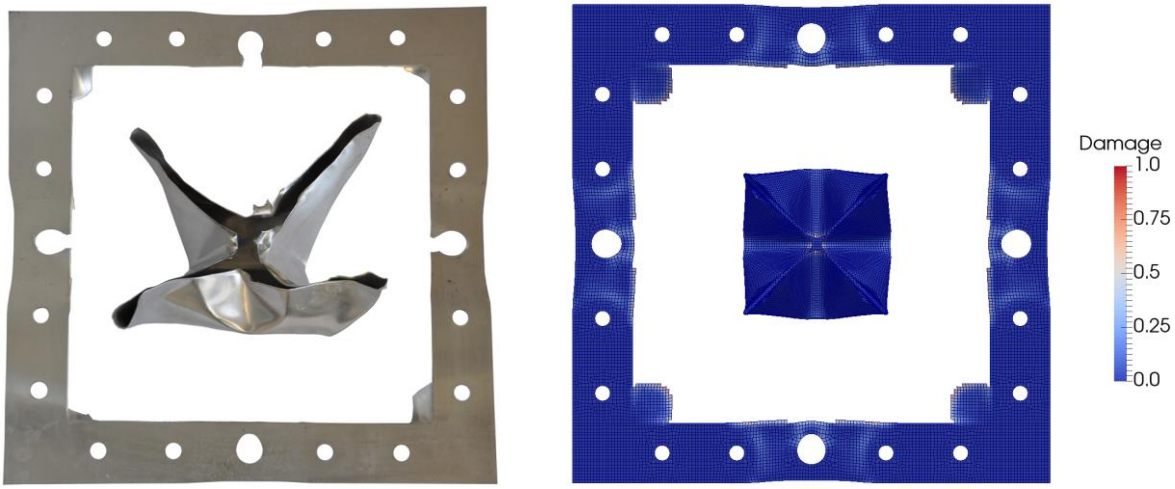

(a) Complete tearing A0

(b) Complete tearing A0

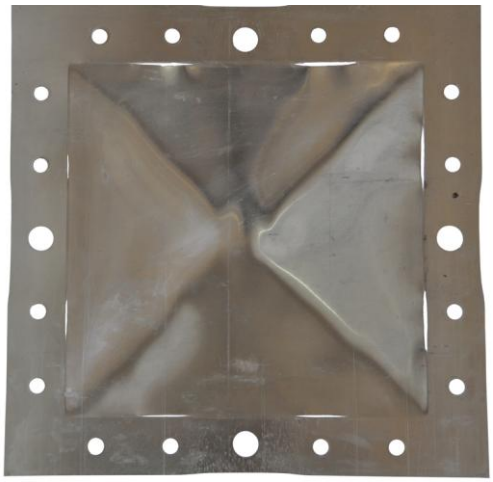

(c) Partial tearing A1

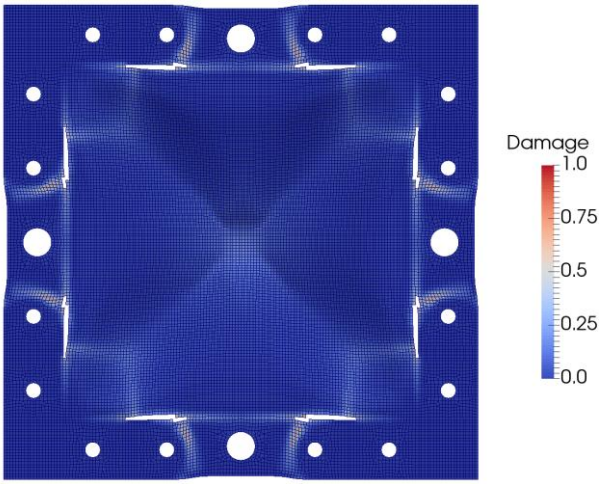

(d) Partial tearing A1

Figure 13. Comparison of experimental (left) and numerical (right) observations on test configurations that experienced failure. Fringe colours represent the contour map of the damage parameter in Eq. (11).

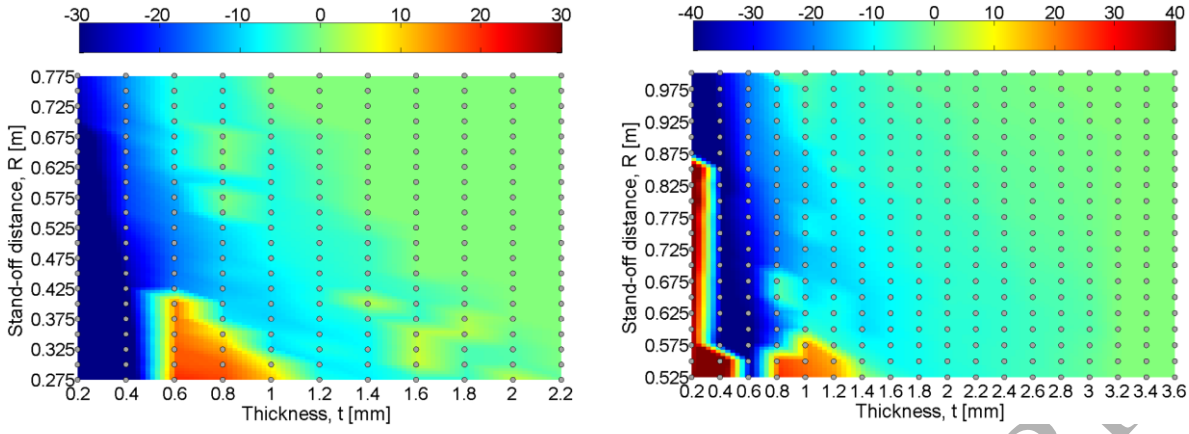

(a) Steel plates (b) Aluminium plates

Figure 14. Blast-structure response spectrum in terms of permanent mid-point deflection. The grey markers illustrate the combinations of stand-off distances and thicknesses used in the numerical simulations to generate the response spectra. The colour scaling indicates the permanent mid-point (out-of-plane) deflection: a red colour indicates a permanent deflection in the same direction as the incoming blast wave, a green colour represents zero permanent mid-point deflection and a blue colour represents CIB.

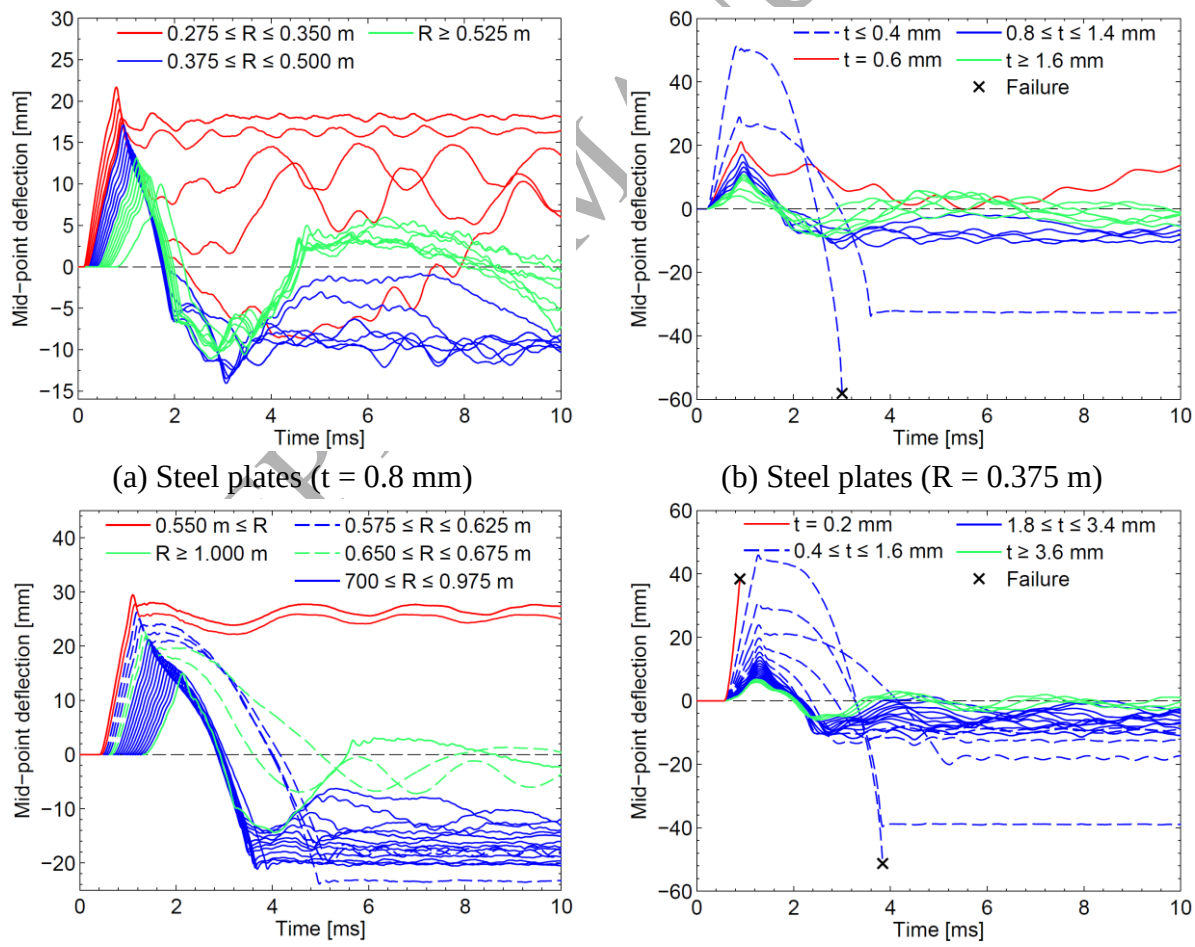

(a) Steel plates (t = 0.8 mm) (b) Steel plates (R = 0.375 m)

(c) Aluminium plates (t = 0.8 mm) (d) Aluminium plates (R = 0.625 m)

Figure 15. Typical mid-point deflection histories for the aluminium and steel plates when varying the stand-off distance and plate thickness.

Table 1. Experimental programme.

Plate thickness [mm]	Stand-off distance, R [m]	Test number 1	2	3	4	5
0.8 (steel plate)	0.125	S11	S12	S13	S14	S15
	0.250	S21	S22	S23	-	-
	0.375	S31	S32	S33	-	-
0.8 (aluminium plate)	0.250	A01	-	-	-	-
	0.375	A11	A12	A13	-	-
	0.500	A21	A22	A23	-	-
	0.625	A31	A32	A33	-	-

Table 2. Experimental and numerical results.

Test	$Z = R/W^{1/3}$ [m/kg$^{1/3}$]*	Experimental data $p_{r\alpha}$ [MPa]	t_{d+} [ms]	$i_{r\alpha+}$ [Ns/m^2]	$d_{z,\max}$ [mm]	Numerical results $p_{r\alpha}$ [MPa]	t_{d+} [ms]	$i_{r\alpha+}$ [Ns/m^2]	$d_{z,\max}$ [mm]	$i_{r\alpha-}$ [Ns/m^2]
S1	0.36	11.5-16.2	0.07	135.7-169.8	33.4	9.5	0.17	161.3	32.0	73.1
S2	0.73	6.8-7.7	0.14-0.17	142.2-168.7	22.3-22.6	6.2	0.54	186.2	23.2	97.9
S3	1.09	3.3-4.9	0.21-0.25	136.2-154.2	15.3-17.2	2.9	0.62	142.6	17.1	84.3
A0	0.73	9.8	0.11	185.7	N/A	6.2	0.54	186.2	N/A	97.9
A1	1.09	3.1-4.3	0.18-0.23	119.5-137.0	41.9-44.4	2.9	0.62	142.6	42.7	84.3
A2	1.46	1.5-1.7	0.35-0.40	99.8-111.5	29.5-32.7	1.4	0.57	109.3	31.0	71.1
A3	1.82	0.8-1.0	0.48-0.54	80.9-83.0	23.8-27.2	0.7	0.60	83.1	23.8	60.1

*Stand-off distance R refers to the respective plate, and not to the sensor located in the frame.

Table 3. Material parameters for the modified Johnson-Cook (MJC) constitutive relation [28].

Material	σ_0 [MPa]	Q_1 [MPa]	C_1 [-]	Q_2 [MPa]	C_2 [-]	c [-]	m [-]	$\dot{p}_0$ [s^{-1}]	W_c [MPa]
Docol 600DL	370.0	236.4	39.3	408.1	4.5	0.001	1.0	5×10^{-4}	473.0
1050A-H14	80.0	49.3	1457.1	5.2	121.5	0.014	1.0	5×10^{-4}	65.0

Table 4. Physical constants for the materials taken from the literature [28].

Material	E [GPa]	ν [-]	ρ [kg/m^3]	C_p [J/kgK]	χ [-]	T_r [K]	T_m [K]
Docol 600DL	210.0	0.33	7850	452	0.9	293	1800
1050A-H14	70.0	0.3	2700	910	0.9	293	893

Table 5. Summary of the numerical results in terms of the maximum deflection-thickness ratios ($d_{z,max}/t$) and total impulses (I_{r+} and I_{r-}) transmitted to the plate from the blast loading. The negative deflection-thickness ratio is given in parentheses for the configurations experiencing CIB.

Test	$d_{z,max}/t$ [-]	I_{r+} [Ns]	I_{r-} [Ns]	CIB
S1	40.0	32.1	12.2	No
S2	29.0	21.0	10.7	No
S3	21.4 (-14.9)	14.0	8.0	Type I
A0	N/A	21.0	10.7	No
A1	53.4	14.4	8.0	No
A2	38.8	10.5	6.5	No
A3	29.8 (-25.1)	7.9	6.0	Type II

*Note that this table reports the total impulses transmitted to the plates, while Table 2 contains the specific impulse recorded by the pressure sensors.